MRI magnetic signature imaging, tracking and navigation for targeted micro/nano-capsule therapeutics

David Folio, Christian Dahmen, Tim Wortmann, M. Arif Zeeshan, Kaiyu Shou, Salvador Pane, Bradley J. Nelson, Antoine Ferreira, Sergej Fatikow

MRI Magnetic Signature Imaging, Tracking and Navigation for Targeted Micro/Nano-capsule Therapeutics

David Folio, Christian Dahmen, Tim Wortmann, M. Arif Zeeshan, Kaiyu Shou, Salvador Pané, Bradley J. Nelson, Antoine Ferreira and Sergej Fatikow

***Abstract*— The propulsion of nano-ferromagnetic objects by means of MRI gradients is a promising approach to enable new forms of therapy. In this work, necessary techniques are presented to make this approach work. This includes path planning algorithms working on MRI data, ferromagnetic artifact imaging and a tracking algorithm which delivers position feedback for the microdevice and a propulsion sequence to enable interleaved magnetic propulsion and imaging. Using a dedicated software environment integrating path-planning methods and real-time tracking, a clinical MRI system is adapted to provide this new functionality for potential controlled interventional targeted therapeutic applications. Through MRI-based sensing analysis, this paper aims to propose a framework to plan a robust pathway to enhance the navigation ability to reach deep locations in human body. The proposed approaches are validated with different experiments.**

I. Introduction

Currently, Magnetic Resonance Imaging (MRI)-based medical micro-/nano-robotic platforms are investigated to reach locations deep in the human body while enhancing targeting efficacy. A recent breakthrough in interventional MRI-guided in vivo procedures demonstrated that real-time MRI systems can offer a well-suited integrated environment for the imaging, tracking, and control of a ferromagnetic device, which was done in the carotid artery of a living swine [1]. These successful experiments pointed out critical challenges in terms of real-time imaging, tracking and navigation for future therapeutic applications, that are controlled targeted drug delivery in brain [2], navigable magnetic carriers for implantable biosensors or controlled ultrasensitive imaging for early diagnosis and treatment of diseases [3].

Recent development of various ferromagnetic filled carbon nanotubes has stimulated the research on their applications in diverse fields. Especially, carbon nanotubes filled with ferromagnetic core are considered to be the most important building blocks for nanomedicine applications [4], [5]. For instance, they have the potential to carry drugs into the organism as they are much smaller than the blood cells and can be easily functionalized by means of a broad range of chemical methods [6]–[8]. For these reasons, in this work ferromagnetic nanowire (NW)-filled multiwalled carbon nanotubes (FMWNT) were designed. Dynamic tracking of ferromagnetic materials are mostly used due to significant magnetic susceptibility artifacts when present inside the MRI during imaging [9]. Moreover, image acquisition delays offer a great challenge for real-time interventional MRI. In [10], the authors demonstrate a new concept of magnetic signature selective excitation tracking (MS-SET) providing high position update rate. However, the poor position accuracy of the MS-SET tracking technique induces navigation or trajectory control errors over pre-planned paths [11]. In contrast, few works address the robust navigation planning problem, that in our context is dealing with the MRI constraints. As improvement, this paper reports on the MRI-based planning and sensing of micro/nano-devices aiming to navigate within vessels. More precisely, the motivation of this paper is to propose a framework to plan a *robust* pathway, wrt. MRI-based tracking capabilities to enhance the navigation ability to reach deep locations in the human body. Through a specially developed software environment integrating path-planning methods and real-time tracking, a clinical MRI system is adapted to provide new functionality for controlled interventional targeted therapeutic applications.

The paper is organized as follows. We first describe the experimental setup using a clinical MRI System. Section III introduces the navigation path planning approach. The MRI artifact imaging and the ferromagnetic nanowire designed as payload for the microcapsule are described in section IV-A. Then, the tracking procedure and the pathway robust to uncertainty are described. Finally, the last section shows the obtained experimental results.

II. Experimental MRI System Description

A clinical 3.0T Siemens Verio MRI platform is used here for planning, imaging, tracking and propulsion of a micro/nanocarrier. A MRI-based navigation system requires observation of the scene in order to either plan the trajectory by off-line mapping, or to correct the device pose error online between the planned and the observed trajectory. To ensure a smooth conveyance of the capsule to its destination, while avoiding collisions and the risk to be trapped in wrong pathways, navigation performance will be affected by external perturbations and MRI technological constraints (such as nonnegligible pulsatile flow, limitations on the magnetic gradient amplitude, MRI overheating avoidance, etc.). Moreover, the overall concept of the MRI-tracking system is based on the fact that both tracking and propulsion are possible with the manufacturer-supplied gradient coils of the MRI system. At any instant only one of the functions

D. Folio and A. Ferreira are with the Institute PRISME EA 4229; ENSI de Bourges, 88 boulevard Lahitolle, 18020 Bourges, FRANCE;

M. A. Zeeshan, k. Shou, S. Pané and B. Nelson are with the Multi-Scale Robotics Lab, Institute of Robotics and Intelligent Systems, ETH Zurich, Zurich, Switzerland;

C. Dahmen, T. Wortmann and S. Fatikow are with the Division Microrobotics and Control Engineering, University of Oldenburg, 26129 Oldenburg, Germany;

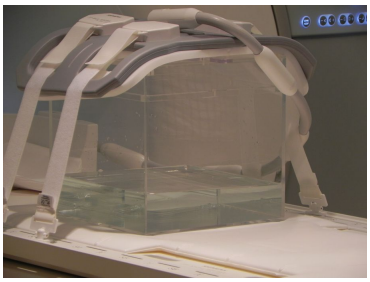

(a) Experimental setup with the square acrylic box under a clinical 3.0T Siemens Verio MRI.

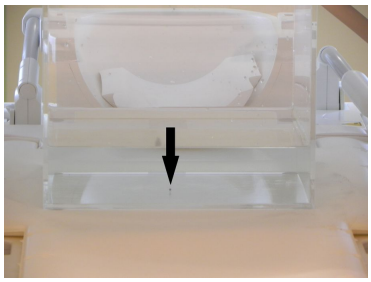

(b) Steel ball (with 2.5mm diameter) inside the box, marked by an arrow

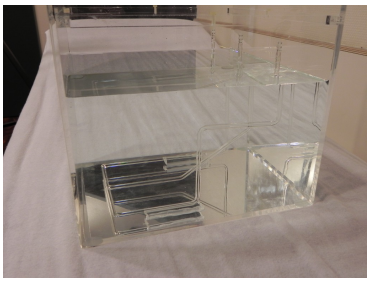

(c) The "phantom" acrylic box with tubular structure.

Fig. 1. The experimental setup for the combined planning and tracking experiments

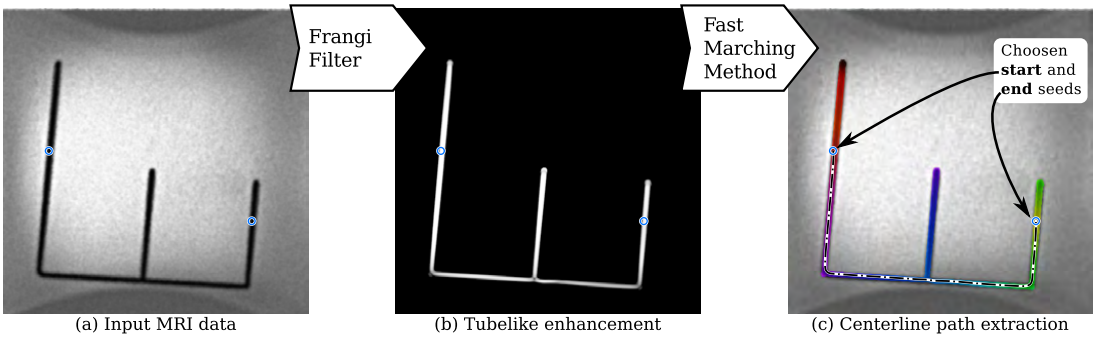

(a) Input MRI data (b) Tubelike enhancement (c) Centerline path extraction

Fig. 2. Navigation path extraction processing: a) MRI slice of the "phantom" acrylic box (tubular structure appear in dark); b) Computed cost function using Frangi filter (tubular structure appear in bright); c) Centerline path between chosen seeds using FMM, with the corresponding front propagation (or equivalently the distance map to reach the target).

could be applied (i.e. either tracking or propulsion), but both will be executed over the same MRI interface. The MRI interface has therefore to be shared and a time-division-multiple-access scheme for it has to be developed. In this work we will focus on the planning and tracking process.

To conduct the various experiments, we use a clinical 3.0T Siemens Verio MRI system providing real-time capabilities. Steel balls of different sizes were used and placed in the cube shape acrylic box depicted on Fig. 1(b). The acrylic box was filled with water and put into the bore of the clinical MRI platform, as shown on Fig. 1(a).

III. Navigation Planning

To allow our microdevice to navigate properly within a tubular structure network we first need to find a *valid* pathway between a initial and final states. The path planning problem has been studied for ages by mathematicians, and has been solved numerically using graph theory or dynamic programming. Among proposed methods are the breadth-first search, heuristic search and hybrid search that are very popular in path planning (such as Dijkstra or A* algorithms). Sethian [12] has illustrate that Dijkstra's method (and by generalization A*) is inconsistent with the underlying continuous problem: the resultant minimal path is bounded to the discrete grid. In opposition, with a similar complexity to common graph-search techniques, Sethian has proposed the Fast Marching Methods (FMM) which converges to a smooth solution in the continuous domain even when it is implemented on a sampled environment [12]. Moreover the FMM needs a very simple initialization (see Fig. 8) and leads to global minimum of a snake-like energy, thus avoiding local minima. Therefore, our proposed planner is built upon the Fast Marching minimal path extraction framework set out in [12] [13]. However, choosing an appropriate and efficient cost function c which drives the front propagation efficiently is the most difficult part of the entire process. In our previous work [14], [15] we have described a framework allowing to find a *minimal centered navigation path*, where a cost function $c_{\texttt{Tub}}$ could be defined as follow:

$$c_{\texttt{Tub}} : \mathbf{x} \in \mathcal{C} \mapsto \texttt{Enhance}(\mathbf{x}) \in \mathbb{R}^+ \tag{1}$$

where $\mathcal{C}$ is the input MRI data, `Enhance` is a tubelike enhancement function. To design the `Enhance` function we use some *a priori* knowledge about tubiform shape and intensity in MRI data. In this context, a typical cost function is designed by using a Frangi filter [16]. This filter computes for a voxel a pseudo-probability of belonging to a tubular structure using geometric properties of the image given by the Hessian matrix. Therefore, this measure highlights tubular structures in the image: with high values inside and nearly zero outside (see Fig. 2(b)). Finally, this approach allows to find a *minimal centered navigation path* between the start and target seed. We have applied this procedure to different sets of data, in 2D [14] as well as in 3D [15]. In this work we have considered a 2D slice of a "phamtom" acrylic box with tubular structure representing a vessel (ie.

artery) network depicted on Fig. 1(c). The corresponding centered navigation path extraction procedure is illustrated on Fig. 2. Nevertheless, the cost function c_{Tub} (1) is based only on spatial interpretation of the MRI data. In the following, we first describe the MRI artifact imaging, and the tracking procedure, and then we will propose to extend the navigation path extraction framework to incorporate a simulation of the microdevice's tracking process.

IV. MRI-BASED SENSING

A. MRI susceptibility artifact imaging

Since the beginning of MRI, the occurrence of magnetic susceptibility artifacts has been studied. In clinical practice, the focus is usually on avoiding artifacts and producing correct images of anatomical structure [17]. In the targeted system, susceptibility artifacts caused by the ferromagnetic microrobotic device will be exploited for position determination. For this purpose, the imaging parameters and artifact formation principles have been investigated.

The image acquisition procedure applied in MRI relies on the presence of a strong homogeneous main magnetic field B_0 and three well-defined gradient fields. Insertion of magnetic material into the field of view clearly violates the assumption of homogeneity. This has mainly two impacts:

- *Intravoxel Dephasing:* Spins inside a single voxel are dephased due to field inhomogeneity, this leads to a damping or loss of signal.
- *Spatial misregistration:* The spatial coding scheme is corrupted and signals are registered incorrectly, causing bright fringes around metallic objects.

An actual artifact shape depends on several factors related to the magnetic object and the imaging sequence. Saturation magnetization and object volume are the most important object specific parameters. For small aspect ratios, object shape is of minor importance. The most important sequence dependent parameters are echo type (gradient echo or spin echo) and echo time. Generally, gradient echo sequences produce much larger artifacts than spin echo sequences, in terms of affected volume. This is due to their inability to compensate temporally constant field inhomogeneities.

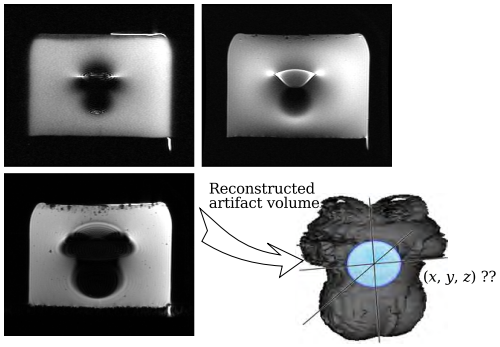

Fig. 3. MRI susceptibility artifact imaging experiment. Results for a 2.5 mm steel sphere, embedded into agarose gel: SSFSE sequence (top left), conventional SE (top right), conventional GE (lower left) and reconstructed artifact volume of GE (lower right).

The imaging parameters have been studied by experiment using a General Electric Signa 3T clinical MRI scanner (for details see [18]). A 2.5 mm steel sphere has been embedded into a 2000 ml container of agarose gel which produces a homogeneous background signal. A representative selection of imaging sequences has been tested: conventional *gradient echo (GE)*, conventional *spin echo (SE)* and the real-time sequence *single-shot fast spin echo (SSFSE)*. The artifacts have been segmented using the *expectation maximization (EM)* algorithm [19]. Sample scans taken from the imaging experiments and the segmentation results for the GE sequence can be seen in Fig. 3. The artifact observed in the GE sequence shows the highest dimensions. Highest signal peaks are found using the conventional SE sequence. SSFSE produces the least severe artifacts. It has to be noted, that the artifact dimensions are orders of magnitude above the object dimensions. From the segmented susceptibility artifacts centroid, the object location can be concluded using a fixed offset vector. This position serves as the initialization position for the tracking procedure described in the section IV-C.

Let us recall that the aim of our MRI driven approach is the control of agglomerated nanoparticles. Subsequently, new nanoparticles have been designed wrt. magnetic steerability and artifact imaging. We describe in the sequel this new nanocarrier design.

B. Application-specific Nanoparticles

The artifact imaging has been verified also using a ferrofluid containing nanoparticles of 10 nm size, and the artifact characteristics have been found equivalent (see Fig. 4(b)). Specifically, ferromagnetic nanowire (NW)-filled multiwalled carbon nanotubes (FMWNT) were designed by using template-assisted growth on silicon. In our process, anodized aluminum oxide (AAO) templates were self-assembled on silicon surface with a diameter of 65-100 nm. Pulsed electrodeposition (PED) was carried out to grow nickel NW inside AAO pores. After PED process, chemical vapor deposition (CVD) was utilized to grow carbon nanotubes inside AAO templates by encapsulating Ni nanowires.

1) Anodic alumina oxide templates: Before anodization, thin layers of Ti, Au and Al were evaporated on Si from bottom-to-top, respectively. Arrays of porous alumina can be obtained by means of anodization. The pores dimensions can be tuned by modifying the electrochemical parameters

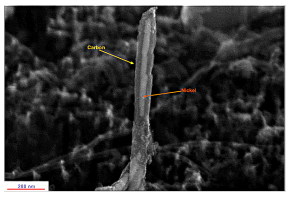

(a) The carbon nanotube

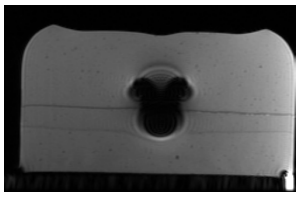

(b) The ferrofluid artifact

Fig. 4. FMWNT with a shell thickness of around 30 nm and agglomeration artifact of an agglomeration of 10 nm iron oxide nanoparticles.

such as electrolyte concentration, voltage, temperature, the oxidation time and subsequent etching treatment [20], [21].

AAO templates with uniform and parallel porous structure are obtained by anodic oxidation of aluminum in a solution of 0.3 M oxalic acid at a constant potential of 40 V.

2) Electrodeposition of Ni nanowires: Eletrodeposition is a common technique for the synthesis of 1D nanostructures and does not require expensive instrumentation, high temperatures or low-vacuum pressures. In PED electric pulses are passed through the electrolyte of metallic ions and nanowires are deposited inside the pores due to reduction of ions. An electrolyte containing nickel salts and other additives was used to deposit Ni nanowires [21], [22].

3) Growth of ferromagnetic filled multiwalled carbon nanotubes (FMWNT): CVD is a convenient method for the synthesis of different types of CNTs ranging from single-walled to multi-walled carbon nanotubes [23]–[25]. The method is suitable to produce large quantities with satisfactory quality and allows also a scaling-up with moderate cost for industrial mass production. In the CVD process, chemical reactions take place, which transforms hydrocarbon precursors into a solid CNT walls on the surface of a substrate. The process is a catalytic process where a catalyst (in this case a transition metal) is involved to control the kinetics of reactions such as the decomposition of the precursor.

The Ni-filled CNTs were grown with a methane (CH4) precursor gas in CVD system (Centrothermo ATV PEO 603) at 850°C. We found that the nickel filling was distributed into several parts with the total length 200 to 400 nm. The diameter of the filling varied from 40 to 60 nm. The carbon layer was about 30 nm thick.

C. Artifact Tracking

Our objective in this section is to track the position of a a microdevice either in 2D or 3D. Due to the characteristic shape of the artifact (see Fig. 3), the particle can be located in the image in most cases by executing template matching. For this, during the recognition phase a template is extracted which will subsequently be used for tracking. The template matching approach chosen is based on correlation. With a template T and the input image I in the 2D case we have:

$$\mathbf{C}(x_p, y_p) = \sum_{x=0}^{x_t} \sum_{y=0}^{y_t} I(x_p + x, y_p + y) \cdot T(x, y) \quad (2)$$

The artifact's position depicted in the template is then derived from the maximum position inside the correlation matrix: $\mathbf{C}(x_\mathrm{o}, y_\mathrm{o}) = \max(\mathbf{C})$. The position of the maximal value in $\mathbf{C}$ corresponds to the position of the tracked object, and the center of gravity of the object can be computed.

1) Three Dimensional Tracking Algorithm: In order to determine the three-dimensional (3D) position of the artifact corresponding to the device, a correlation is applied with a template stack to deliver the third dimension coordinate. The approach used involves multiple correlation templates, which will be subsequently used and the best match determined. The principle of the algorithm can be seen in Fig. 5.

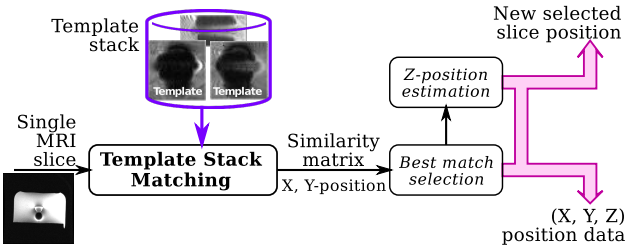

Fig. 5. The three dimensional tracking algorithm

A template stack T_n is used for correlation. The resulting correlation matrices $\mathbf{C}_n$ are then analyzed for their maximum:

$$\mathbf{C}_n(x_\mathrm{o}, y_\mathrm{o}) = \max(\mathbf{C}_n) \quad (3)$$

and the best fitting matrix is determined:

$$\mathbf{C}_\mathrm{fit} = \max(\mathbf{C}_n) \quad (4)$$

The fit is then further refined by interpolation, and a segmentation with size analysis is used to improve the results.

D. Experiment Description and Sensing Results

To evaluate the efficiency of the tracking algorithm, experiments have been executed in a clinical MRI system, illustrated in Fig. 1(a). A steel ball was positioned in the center of the box with a special mechanism after the box has been driven into the system, to prevent earlier movements due to the strong static magnetic field gradients during insertion. The steel ball can be seen marked by an arrow in Fig. 1(b). Hence, the tracking process uncertainty has been evaluated. For this, steel balls of different sizes have been fixed and repeatedly scanned in static case. The imaging sequences used for this were a HASTE sequence, and a FLASH sequence. The results for the experiment are summarized in table I. As can be seen, the standard deviation (std) of the extracted positions is mostly better when using the FLASH sequence. No clear dependency on size can be observed. Generally, the std lies below 0.2 voxels, which in this case with the voxel spacings from the sequence parameters delivers a standard deviation well below 200 μm.

TABLE I
STANDARD DEVIATIONS IN X (std(X)) AND Y (std(Y)) DIRECTIONS FOR THE TRACKING ALGORITHM

Size (mm)	Sequence	std(x) [voxels]	std(y) [voxels]	std(x) (mm)	std(y) (mm)
0,7	HASTE	0,080	0,043	0,100	0,053
1,5	HASTE	0,127	0,127	0,159	0,159
2,0	HASTE	0,116	0,098	0,144	0,123
3,0	HASTE	0,042	0,044	0,053	0,055
0,7	FLASH	0,036	0,054	0,042	0,063
1,5	FLASH	0,036	0,054	0,042	0,063
2,0	FLASH	0,047	0,061	0,055	0,071
3,0	FLASH	0,166	0,158	0,194	0,185

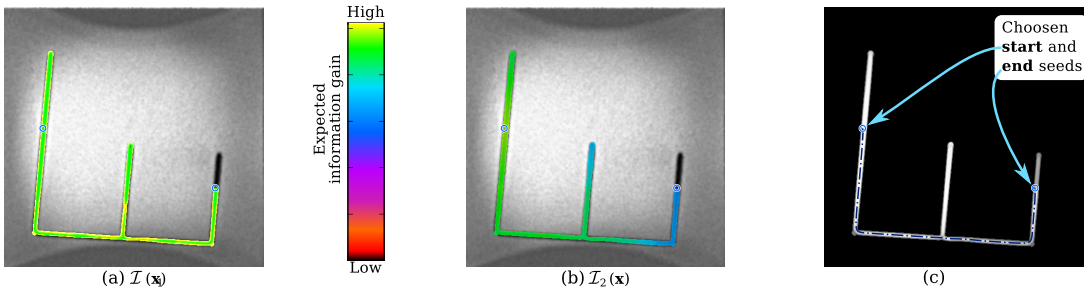

Fig. 6. Cost map function and extracted path in presence of uncertainty: a) $\mathcal{I}_1(\mathbf{x})$ using an uniform sensor model propagation; b) $\mathcal{I}_2(\mathbf{x})$ using an attenuated sensor model propagation; c) isotropic cost function c_T.

V. Planning with Uncertainty

There are several important sources of uncertainty which should be considered in MRI-based navigation planning. These include uncertainty in MRI data acquisition and processing, carrier model and position tracking. Failure to account for these uncertainty in the planning method could result in trapping the device in a wrong tube segment. In our context we have to ensure efficient sensing capability with a low level of uncertainty. For that, we simulate in real-time the microdevice's tracking process in order to assess each candidate configuration wrt. a sensing objective.

Our goal is to define a navigation path that maximizes the likelihood of successful execution by ensuring that sensor information can be gathered at all crucial stages. Therefore, our aim is to define a new cost function $c_{\texttt{Bel}}$ that maps the system's belief in its position $\mathbf{x}$ wrt. a sensor model.

$$c_{\texttt{Bel}} : \mathbf{x} \in \mathcal{C} \mapsto \mathcal{I}(\mathbf{x}) \in \mathbb{R}^+ \tag{5}$$

One way to design such a map (5) is to use the Sensor Uncertainty Field (SUF) introduced in [26]. The SUF allows to define a mapping from a state $\mathbf{x}$ to an expected information gain $\mathcal{I}(\mathbf{x})$. This expected information gain (or, equivalently, the expected entropy reduction) quantifies the microdevice's ability to localize itself at different positions $\mathbf{x}$ in $\mathcal{C}$: locations with high $\mathcal{I}(\mathbf{x})$ correspond to locations that generate sensor measurements that we *expect* to maximize the tracking process accuracy. In the SUF framework, $\mathcal{I}(\mathbf{x})$ is computed, given an observed data $\mathbf{y}$, from the difference in Shannon entropy of the prior and posterior distributions:

$$\mathcal{I}(\mathbf{x}) = H(p(\mathbf{x})) - H(p(\mathbf{x}|\mathbf{y})) \tag{6}$$

where the Shannon entropy of a probability distribution $p(\mathbf{x})$ is defined as: $H(p(\mathbf{x})) = -\int p(\mathbf{x}) \log p(\mathbf{x})\, d\mathbf{x}$. The prior entropy $H(p(\mathbf{x}))$ provides a measure of the certainty on the carrier's belief in its position $\mathbf{x}$, before the sensory input $\mathbf{y}$ is received. $H(p(\mathbf{x}|\mathbf{y}))$ denotes the expected entropy change after measurement data $\mathbf{y}$. The posterior probability $p(\mathbf{x}|\mathbf{y})$ is classically given by Bayes' rule: $p(\mathbf{x}|\mathbf{y}) = \frac{p(\mathbf{y}|\mathbf{x})p(\mathbf{x})}{p(\mathbf{y})}$, where $p(\mathbf{y})$ is the likelihood of observing data $\mathbf{y}$, and $p(\mathbf{y}|\mathbf{x})$ is the likelihood of sensing data $\mathbf{y}$ at state $\mathbf{x}$. $p(\mathbf{y}|\mathbf{x})$ is computed from the sensor model and the observed scene. The path that minimizes the uncertainty is then the one that maximizes $\mathcal{I}(\mathbf{x})$.

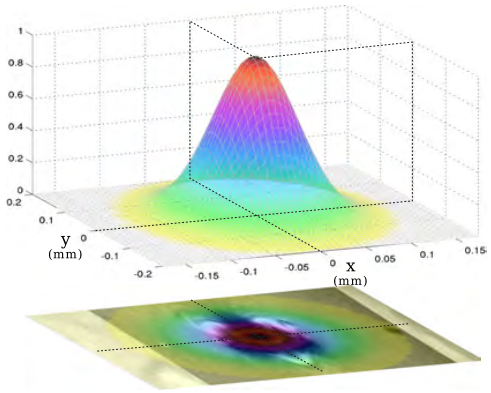

Fig. 7. Tracking process modeled as a white multivariate-Gaussian distribution.

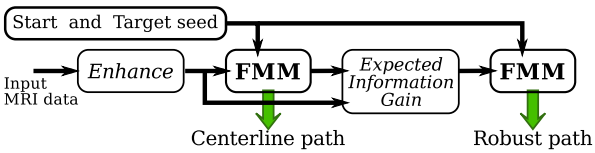

Fig. 8. Navigation path extraction procedure robust to sensing uncertainty.

A. Application and Results

In order to calculate the prior entropy $H(p(\mathbf{x}))$, we need a probabilistic model for the physical space. To this aim we use our *a priori* knowledge, that is: each (unknown) state $\mathbf{x}$ must be within the tubular structures. Therefore, as previously introduced, $\texttt{Enhance}(\mathbf{x})$ could be seen as a pseudo-probability for the device of belonging to a tubular structure, and leads to: $p(\mathbf{x}) \propto \texttt{Enhance}(\mathbf{x})$. To compute $H(p(\mathbf{x}|\mathbf{y}))$, we assume that the sensing process could be modeled by a white multivariate-Gaussian distribution: $\mathcal{N}(0, \Sigma^2_{\mathbf{y}})$, with zero mean and $\Sigma^2_{\mathbf{y}}$ the covariance matrix. To evaluate the efficiency of our proposed approach, we have considered a FLASH sequence tracking process of a 0.7mm steel ball. Thus the covariance matrix $\Sigma^2_{\mathbf{y}}$ of the Gaussian sensor model is computed using the table I, and is shown on Fig.7. The sensor model has to be propagated over all states $\mathbf{x}$. As this propagation could be not computationally efficient, we reduce the computation space to the level set provided by the FMM front propagation using $c_{\texttt{Tub}}$ (1). Moreover, it provides an expected information gain bounded by the

tubular shape. Finally the secondary FMM step is executed to get a pathway that maximizes $\mathcal{I}(\mathbf{x})$ within the tubular structure. This new navigation path extraction procedure is *robust* to uncertainties as illustrated in Fig. 8

Fig. 6.a shows the corresponding computed expected information gain $\mathcal{I}_1(\mathbf{x})$ and the resulting navigation path. As one can see, $\mathcal{I}_1(\mathbf{x})$ is uniformly distributed within the the tubular structure. However, this does not correspond to the real case: the tracking action could not be performed in each state due to the MRI time-multiplexing constraints (see [14], [15] for further details). Thus, to consider the tracking attenuation effects, we use the distance map from the initial state $\mathbf{x}_0$ provided by the FMM (see Fig 2(c)) to improve the sensor model $p(\mathbf{y}|\mathbf{x})$. This leads to the secondary information gain map $\mathcal{I}_2(\mathbf{x})$ depicted on Fig. 6.b.

Finally, the pathway based only on uncertainty, overestimates the navigation path leading to inconsistencies such as e.g., tube wall countouring or tube crossing. In such a case, a solution is to compute a weighted sum between the cost functions based on spatial information $c_{\texttt{Tub}}$ (ie. using the Frangi filtering) and based on expected information gain $c_{\texttt{Bel}}$, that is:

$$c_T = \lambda_1 c_{\texttt{Tub}} + \lambda_2 c_{\texttt{Bel}} \tag{7}$$

where λ_1 and λ_2 are weighting factors. Hence, this new cost function formulation allows to tune the navigation path to be either a centerline path or maximizing the expected information gain. Fig. 6.c presents a pondered pathway extracted using $\mathcal{I}_2(\mathbf{x})$ and with $\lambda_1 = 0.66$ and $\lambda_2 = 1 - \lambda_1$.

VI. Experimental Results

To validate the above mentioned MRI-based navigation and tracking procedure, we implemented a simple propulsion procedure and applied them in the clinical MRI system. During the experiment, different motions have been executed, and the corresponding images taken as shown on figures 9.

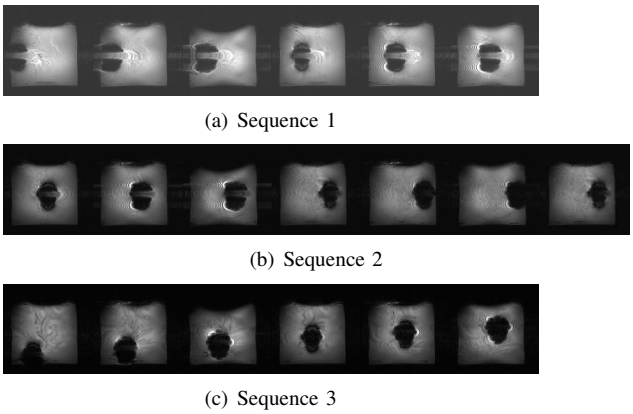

(a) Sequence 1

(b) Sequence 2

(c) Sequence 3

Fig. 9. Sequences recorded with movement in X-direction (upper two) and diagonal displacements (lowest)

The templates used for these image sequences are shown in Fig. 10. It can be seen that the templates differ in characteristics in each sequence. This strengthens the need for recognition and subsequent template extraction from the recognition data.

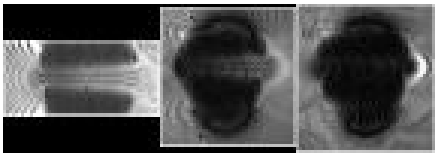

Fig. 10. Templates used for the three sequences

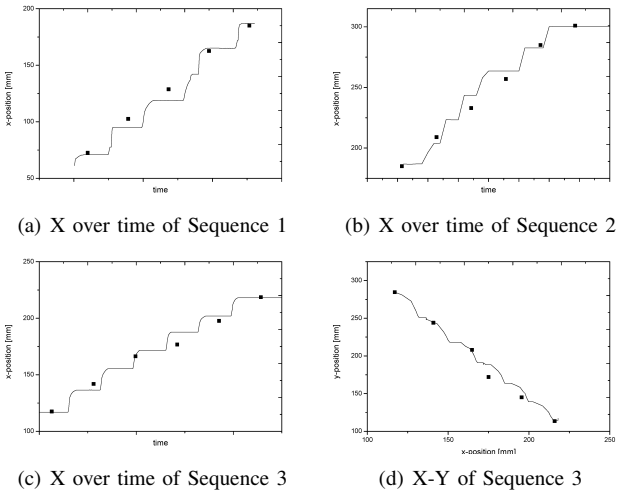

(a) X over time of Sequence 1

(b) X over time of Sequence 2

(c) X over time of Sequence 3

(d) X-Y of Sequence 3

Fig. 11. X-position of the steel ball over time extracted from the sequences, dots: position tracked in MRI images, line: position tracked from video images

As can be seen in Fig. 11, the x-direction motion in the first recorded sequence follows the camera-observed path. It has to be noted though, that only 6 data points were extracted, because of the 6 MRI images taken during the movement. For the second sequence the effect is the same. Also the x-direction motion of the third sequence is in line with expectations. The diagonal path of the third sequence is clearly visible in Fig. 11(d). The magnetic gradient applied here had the same strength for x and y-direction. This is also visible in the tracked data. For comparison, the path of the steel ball during the third sequence tracked in the camera image is also shown. As it can be observed, the movement is close to the MRI tracked movement. Finally, the experiments clearly show that paths are extracted which clearly fit the microdevice displacements. It can be concluded that the tracking algorithm is working, though the accuracy and precision has to be improved still. Improvements are possible by better tailoring of the used imaging sequence and optimization of the necessary parameters like slice spacing.

VII. Conclusions and Future Works

In this paper, we described a framework to extract a robust pathway with respect to MRI-based sensing capabilities. The related dedicated artifact imaging and tracking procedure using a clinical MRI system is presented and evaluated. Sensor feedback for the navigation is extracted by tracking the artifact in the MRI images which are continuously acquired during sequence execution. From preoperative MRI scan data and the characterized sensing model, a reliable pathway is

planned which will be used to control the ferromagnetic nanowire agglomeration through the cardiovascular system to properly reach deep locations in the human body. Each procedure has been experimentally verified using an adapted clinical MRI system.

In subsequent steps, the sensing methods have to be combined with a controller and the closed loop control has to be validated over the planned pathway. Also it has to be shown that this approach works in biologically inspired experimental setups.

VIII. ACKNOWLEDGMENTS

This work was supported by European Union's 7th Framework Program and its research area ICT-2007.3.6 Micro/nanosystems under the project NANOMA (Nano-Actuactors and Nano-Sensors for Medical Applications).

REFERENCES

[1] A. Chanu, O. Felfoul, G. Baudoin, and S. Martel, "Adapting the clinical mri software environment for real-time navigation of an endovascular untethered ferromagnetic bead for future endovascular interventions," *Magnetic Resonance in Medecine*, vol. 59, pp. 1287–1297, 2008.

[2] J. Park, G. von Maltzahn, L. Zhang, M. Schwartz, E. Ruoslahti, S. Bhatia, and M. Sailor, "Magnetic iron oxide nanoworms for tumor targeting and imaging," *Advanced Materials*, vol. 20, no. 9, pp. 1630–1635, 2008.

[3] J. J. Abbott, K. E. Peyer, M. C. Lagomarsino, L. Zhang, L. X. Dong, I. K. Kaliakatsos, and B. J. Nelson, "How should microrobots swim?" *Int. J. of Robotics Research*, Jul. 2009.

[4] A. Leonhardt, I. Moench, A. Meye, S. Hampel, and B. Buechner, "Synthesis of ferromagnetic filled carbon nanotubes and their biomedical application," *Advances in Science and Technology*, vol. 49, pp. 74–78, 2006.

[5] I. Mönch, A. Meye, A. Leonhardt, K. Krämer, R. Kozhuharova, T. Gemming, M. Wirth, and B. Büchner, "Ferromagnetic filled carbon nanotubes and nanoparticles: synthesis and lipid-mediated delivery into human tumor cells," *Journal of magnetism and magnetic materials*, vol. 290, pp. 276–278, 2005.

[6] K. Balasubramanian and M. Burghard, "Chemically functionalized carbon nanotubes," *Small*, vol. 1, no. 2, pp. 180–192, 2005.

[7] Z. Liu, S. Tabakman, K. Welsher, and H. Dai, "Carbon nanotubes in biology and medicine: in vitro and in vivo detection, imaging and drug delivery," *Nano research*, vol. 2, no. 2, pp. 85–120, 2009.

[8] R. Klingeler, S. Hampel, and B. Buchner, "Carbon nanotube based biomedical agents for heating, temperature sensoring and drug delivery," *International Journal of Hyperthermia*, vol. 24(6), pp. 496–505, 2008.

[9] H. Graft, U. Lauer, A. Berger, and F. Schick, "Rf artifacts caused by metallic implants or instruments which get more mrominent at 3t: an in vitro study," *Magnetic Resonance Imaging*, vol. 23, pp. 493–499, 2005.

[10] O. Felfoul, J. Mathieu, G. Beaudoin, and S. Martel, "In vivo mr tracking based on magnetic signature selective excitation," *IEEE Trans. Med. Imag.*, vol. 27, no. 1, p. 2835, 2008.

[11] W. Sabra, M. Khouzam, and S. Martel, "Use of 3D potential field and an enhanced breath-first search algorithms for path-planning of microdevices propelled in the cardiovascular system," *27th IEEE EMBS Annual Int. Conf.*, Apr. 2005.

[12] J. A. Sethian, *Level set methods and fast marching methods: evolving interfaces in computational geometry, fluid mechanics, computer vision, and materials science*. Cambridge university press Cambridge, 1999.

[13] D. Mueller and A. Maeder, "Robust semi-automated path extraction for visualising stenosis of the coronary arteries," *Computerized Medical Imaging and Graphics*, vol. 32, no. 6, pp. 463–475, 2008.

[14] K. Belharet, D. Folio, and A. Ferreira, "Endovascular navigation of a ferromagnetic microrobot using MRI-based predictive control," in *IEEE/RSJ Int. Conf. on Intel. Robots and Systems*, Taipei, Taiwan, Oct. 2010.

[15] ——, "3D MRI-based predictive control of a ferromagnetic microrobot navigating in blood vessels," in *IEEE RAS & EMBS Int. Conf. on Biomedical Robotics and Biomechatronics*, Tokyo, Japan, Sep. 2010.

[16] A. Frangi, W. Niessen, K. Vincken, and M. Viergever, "Multiscale vessel enhancement filtering," *Lecture Notes in Computer Science*, pp. 130–137, 1998.

[17] J. Port and M. Pomper, "Quantification and minimization of magnetic susceptibility artifacts on gre images," *Neuroradiology*, vol. 24, pp. 958–964, 2000.

[18] T. Wortmann, C. Dahmen, and S. Fatikow, "Study of MRI Susceptibility Artifacts for Nanomedical Applications," *Journal of Nanotechnology in Engineering and Medicine*, vol. 1, 2010.

[19] D. A. Forsyth and J. Ponce, *Computer Vision: A Modern Approach*. Prentice Hall, 2002.

[20] M. A. Zeeshan, K. Shou, K. M. Sivaraman, T. Wuhrmann, S. Pané, E. Pellicer, and B. J. Nelson, "Nanorobotic drug delivery: If i only had a heart..." *Materials Today*, vol. 14, no. 1-2, pp. 54 – 54, 2011.

[21] K. Nielsch, F. Müller, A. Li, and U. Gösele, "Uniform nickel deposition into ordered alumina pores by pulsed electrodeposition," *Advanced Materials*, vol. 12, no. 8, pp. 582–586, 2000.

[22] G. Sklar, K. Paramguru, M. Misra, and J. LaCombe, "Pulsed electrodeposition into aao templates for cvd growth of carbon nanotube arrays," *Nanotechnology*, vol. 16, p. 1265, 2005.

[23] M. Kumar and Y. Ando, "Chemical vapor deposition of carbon nanotubes: a review on growth mechanism and mass production," *Journal of nanoscience and nanotechnology*, vol. 10, no. 6, pp. 3739–3758, 2010.

[24] M. Meyyappan, L. Delzeit, A. Cassell, and D. Hash, "Carbon nanotube growth by pecvd: a review," *Plasma Sources Science and Technology*, vol. 12, p. 205, 2003.

[25] H. Sato, T. Sakai, A. Suzuki, K. Kajiwara, K. Hata, and Y. Saito, "Growth control of carbon nanotubes by plasma enhanced chemical vapor deposition," *Vacuum*, vol. 83, no. 3, pp. 515–517, 2008.

[26] H. Takeda and J. Latombe, "Sensory uncertainty field for mobile robot navigation," in *IEEE Int. Conf. on Robotics and Automation*, vol. 3. Nice, France: IEEE, May 2002, pp. 2465–2472.